Appl Phys A (2011) 104:1181–1187
DOI 10.1007/s00339-011-6407-z

Applied Physics A
Materials Science & Processing

Effect of humidity on the a.c. impedance of $CH_3NH_3SnCl_3$ hybrid films

R. Mosca · P. Ferro · T. Besagni · D. Calestani · F. Chiarella · F. Licci

Received: 22 April 2010 / Accepted: 5 April 2011 / Published online: 5 May 2011

Abstract Impedance spectroscopy measurements show that complex conductivity of thermally ablated $CH_3NH_3SnCl_3$ films is strongly enhanced when humidity increases. Coplanar two-electrode test devices are modeled through an equivalent circuit comprising one resistance and two constant phase elements. It is shown that the influence of ambient humidity is mainly resistive. The dynamic responses of the devices to humidification/dehumidification cycles point out that the a.c. current varies by more than three orders of magnitude when humidity is varied between dry air and 80% relative humidity. The rise times are few hundred seconds while fall times are as short as few tens of seconds. This observation suggests that impedance variations are determined by mechanisms involving loosely bound water molecules physisorbed at the surface of the hybrid film. The results obtained are discussed in terms of protonic conduction.

R. Mosca (✉) · P. Ferro · T. Besagni · D. Calestani · F. Chiarella · F. Licci
IMEM-CNR, Parco Area delle Scienze, 37/a, 43124 Fontanini-Parma, Italy
e-mail: mosca@imem.cnr.it
Fax: +39-0521-269206

P. Ferro
e-mail: ferro@imem.cnr.it
Fax: +39-0521-269206

T. Besagni
e-mail: besagni@imem.cnr.it
Fax: +39-0521-269206

D. Calestani
e-mail: calle@imem.cnr.it
Fax: +39-0521-269206

F. Licci
e-mail: licci@imem.cnr.it
Fax: +39-0521-269206

F. Chiarella
CNR-INFM Coherentia, via Cintia snc, 80125 Napoli, Italy
e-mail: fabio.chiarella@na.infn.it
Fax: +39-0521-269206

1 Introduction

The organic-metal-halide hybrid perovskites are currently widely investigated [1], mostly in view of electronic device applications. In these crystalline solids, the structure-properties relationships conveniently correlate, thus providing a mechanism for understanding and tailoring properties. The basic ABX_3 hybrid structure (where A = organic-ammonium cation, B = divalent metal, X = halide) is a network of corner-sharing BX_6 octahedra, with A occupying the 12-fold coordinated sites between the octahedra. If appropriate-size elements (large B and X and small A ionic radii) are combined, compact three-dimensional (3-D) structures result, either cubic or distorted-cubic [2]. Among the 3-D hybrid perovskites, $CH_3HN_3^+$ (methyl ammonium, Ma)- Sn-based halides, $MaSnX_3$, are attracting a lot of attention [3–8] mainly as a consequence of the intriguing electronic conductivity properties. The Sn-based 3-D hybrids show, in fact, a semiconducting or even metal-like character, differently from the homologous (Pb-based, for instance) hybrids, which are insulating [9]. Besides, they can be prepared by using relatively simple and low cost techniques and are well suited for large area deposition on flexible substrates.

The largest part of $MaSnX_3$ literature refers to iodide and bromide hybrid conductivity and the data are collected on pressed powders. A metallic-like conductivity was reported for $MaSnI_3$[4], with a room temperature resistivity, ρ_{RT}, ∼6.5 mΩ cm and a hole mobility ∼50 $cm^2\,V^{-1}\,s^{-1}$.

On the basis of the resistivity vs. temperature behavior, cubic $MaSnBr_3$ is described as a semiconductor [10] having an a.c. $\rho_{RT} \approx 4.2 \times 10^3\ \Omega$ cm [6], about 10 times larger than the d.c. ρ_{RT} [10]. Such a discrepancy has been ascribed to processes involving electric contact potentials and grain-boundary effects. $MaSnBr_3$ pellets were also found to undergo a semiconductor-insulator transition at about 230 K, corresponding to the cubic-rhombohedral phase transition [6]. Yamada et al. [7] measured the conductivity of $MaSnCl_3$ pressed powders by a complex impedance method and obtained $\rho_{RT} \approx 1.25 \times 10^5\ \Omega$ cm, higher than the resistivity of both $MaSnI_3$ and $MaSnBr_3$. The authors observed that the a.c. conductivity monotonically increased with increasing temperature and suggested that $MaSnCl_3$ is semiconductor in the 290–480 K temperature range, in spite of the occurrence of three structural phase transitions (cubic→rhombohedral→monoclinic→triclinic) at $T = 463$, 331, and 307 K, respectively.

To the best of our knowledge, only very few measurements [5, 11] were reported dealing with the electrical properties of $MaSnI_3$ and $MaSnBr_3$ films and no any was found relevant to $MaSnCl_3$ film. In particular, at the cubic-orthorhombic transition temperature $MaSnBr_3$ films were reported to show only a smooth change in the conductivity dependence on T [11]. Furthermore, when comparing the transport characteristics of powders and films with the same nominal composition, significant discrepancies result [4–7, 10, 11], which definitely demonstrate that the transport characteristics are dependent on the sample morphology and history, as well as on the measurement technique. An additional problem in such hybrids is represented by the chemical instability. $MaSnI_3$, for example, was found to be air sensitive and to decompose in air within several hours, unless not stored and manipulated in argon-filled glove box [4].

In the frame of a systematic research to evaluate the potentialities of the hybrid perovskites for applications in optoelectronic technologies, we demonstrated the deposition of high quality $MaSnCl_3$ films and combined optical absorption and structural characteristics with ab-initio calculations [12]. On the same films, we are presently carrying out detailed analyses of the transport characteristics. When measuring the $MaSnCl_3$ films resistivity by the van der Pauw technique, we found a significant dependence on the ambient atmosphere, i.e., conduction could not be measured in dry air or in vacuum, while resistivity decreases to about $6 \times 10^4\ \Omega$ cm when measured under ambient atmosphere. This evidence suggested that the transport characteristics of $MaSnCl_3$ hybrid are significantly affected by humidity, even if literature data neither mention such an aspect nor give any details about the conditions under which the experiments were carried out.

In this report, we describe and discuss the results of impedance spectroscopy measurements performed under different humidity conditions on two-contact test devices based on $MaSnCl_3$ films. We show that, with respect to the speed, magnitude and reproducibility of the response to the humidity variations, $MaSnCl_3$ hybrid may be envisaged as a promising material for humidity sensing.

2 Experimental

100–500 nm thick $MaSnCl_3$ films were simultaneously deposited at room temperature on both bare and Au-metalized glass substrates by the single source thermal ablation technique [13]. Substrates were cleaned by rinsing in hot trichloroethylene, acetone and isopropyl alcohol, and dried in blowing nitrogen. The precursor was polycrystalline $CH_3NH_3SnCl_3$ obtained by evaporating under vacuum a water suspension of CH_3NH_3Cl and $SnCl_2$ in 1 : 1 molar ratio. The film deposition was carried out by the SSTA technique, in a home-tailored ablation apparatus [14]. The optimal deposition parameters were determined by trials and were periodically adjusted, in particular the heating power, and deposition time. Typical deposition parameters are reported in [11]. The substrates were generally kept at room temperature. Films were deposited by passing a large current ($\geq$150 A) through the Ta crucible, thus enabling the thermal ablation of the precursor from the liner toward the substrate. The deposition process was accomplished in few seconds and an almost instantaneous ablation occurred. The film thickness was measured by a standard profilometer and found to be qualitatively related to the used precursor mass. Films considered in the present paper were 380 nm thick.

After the deposition, the structural quality and the stability of the films were confirmed by X-ray diffraction measurements in a Siemens (D500) powder diffractometer, with CuKα radiation.

Electrical measurements were performed using interdigitated two electrode structures where the spacing between the two electrodes was 500 μm. The active area, calculated from the free space between the gold fingers, was 9.75×10^{-2} cm^2. Gold contacts were evaporated in a BOC Edwards electron beam system using a Cr adhesion layer and were defined by standard photolithography and lift off procedures. After electrode deposition, the substrates were rinsed in a piranha solution (97% H_2SO_4/30% H_2O_2 = 3/1) to give a fresh gold surface. The use of a shadow mask allowed hybrid depositions to be aligned to the gold electrodes. The resulting test devices (hereafter called "devices" for the sake of brevity) were mounted on TO-8 headers and electrically connected by 25 μm thick gold wires ultrasonically bonded at room temperature in a Hybond 626 bonder.

The electrical characteristics of the devices as a function of the relative humidity (RH) were measured at constant temperature (25 ± 2°C) in a measurement chamber where

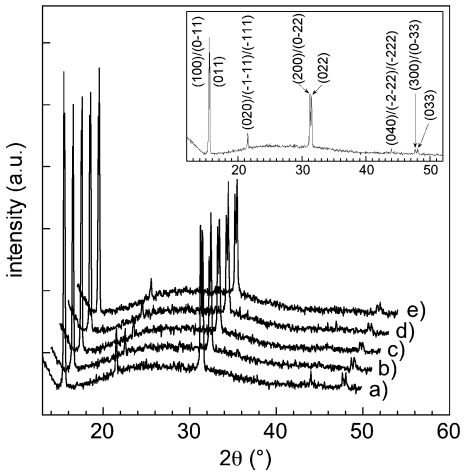

Fig. 1 X-ray diffraction patterns of a typical $MaSnCl_3$ hybrid film on glass substrate. The patterns were sequentially taken before hybrid exposure to humidity (**a**), after 24 (**b**), and 72 (**c**) hours under humidification/dehumidification cycles between RH = 25% and RH = 80%, and after further 48 hours (**d**), and 3 weeks (**e**) in ambient air (25% ≤ RH ≤ 55%). In the *inset*, the peak indexing is reported, within the P1 space group of the triclinic system [7]

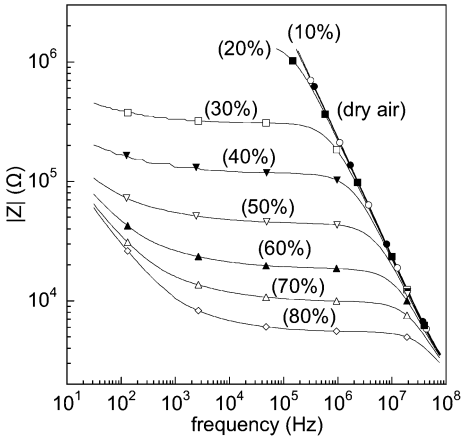

Fig. 2 Impedance magnitude $|Z|$ measured as a function of frequency at different RH values: dry air (●), 10% (○), 20% (■), 30% (□), 40% (▼), 50% (▽), 60% (▲), 70% (△), 80% (◇)

RH was adjusted in the 0–80% range by two mass flow controllers that allowed water-saturated air (synthetic air saturated with water vapor by bubbling in a humidifier) to be mixed in the proper ratio with synthetic air dried by a silica gel filter. Under stationary humidity conditions RH instability range was about ±1.5%, as measured by a Honeywell HIH-4000-001 humidity sensor set close to the sample.

Impedance spectroscopy measurements were performed in the 5 Hz–13 MHz frequency range, using a Hewlett Packard 4192A impedance analyzer. 250 mV signal amplitude and 0 V d.c. bias were used for all the measurements.

The response characteristics of the devices were tested by applying an a.c. stimulus (Root Mean Squared Voltage $V_{ac} = 0.21$ V) through an Ortec 9473 signal source. I_{ac} current was measured as a function of time by a Femto DLPCA-200 current amplifier connected to a Keithley 2000 multimeter.

3 Results and discussion

The X-ray diffraction patterns taken on the just deposited hybrid, before exposing them to humid air, (Fig. 1) prove that the films are perovskite single-phase and well crystallized within the triclinic system (P1 space group), consistently with the description of Yamada et al. [7]. The films exhibit preferential crystallographic orientations,pointed out by the occurrence of the (0kk) and (h00)/(0-kk) reflection sets in the diffraction patterns. Less intense reflections at $2\Theta \approx 21.5°$ and ≈40° can be indexed as (02k0)/(–hhh)/(-h-hh). The presence of gold contacts under the film does not modify the diffraction patterns with respect to films deposited on glass substrates. In order to assess the stability of the hybrid when it is exposed to humid air, X-ray diffraction measurements were sequentially carried out on the same film after 72 hours humidification/dehumidification cycles with RH ranging between 80% and 30%, and after 21 days in ambient atmosphere with RH comprised in the 25%–55% range (Fig. 1). The diffraction patterns, i.e., peak shape and height, remain almost unchanged within the experimental uncertainty, thus indicating that $MaSnCl_3$ films are stable under the considered experimental conditions, in contrast to $MaSnI_3$ films that decompose in air within some hours [4].

The dependence of the impedance magnitude, $|Z|$, on the stimulus frequency, f, is shown in Fig. 2 for various RH values. Under dry-air conditions the impedance falls off as f^{-1} over the examined frequency range, so that a capacitance value of about 4 pF could be deduced. This capacitance can be seen as the vacuum capacitance, C_0, of the sample holder and coplanar electrode arrangement, since its value is well consistent with the 3.6 pF value we measured on the same contact structure in the absence of the hybrid film. When humidity increases (RH ≥ 30%), the dependence of $|Z|$ on frequency shows three main features (Fig. 2): (i) at high frequencies $|Z|$ exhibits the described f^{-1} behavior, that is almost independent of RH, (ii) at intermediate frequencies $|Z|$ varies very slowly with ω indicating that a resistive-type behavior of the film is dominant, and (iii) at low frequencies $|Z|$ increases with decreasing f. It is worth noting that humidity influences the devices impedance mainly in the intermediate frequency range.

In order to achieve an overview of the conduction processes involved in the device response, we plot the impedance data in the so-called Nyquist diagram (imaginary, Z'', vs. real, Z', impedance) (Fig. 3). In the high frequency range complex, impedance spectra comprise a single skewed semicircle whose diameter increases when RH decreases, so that

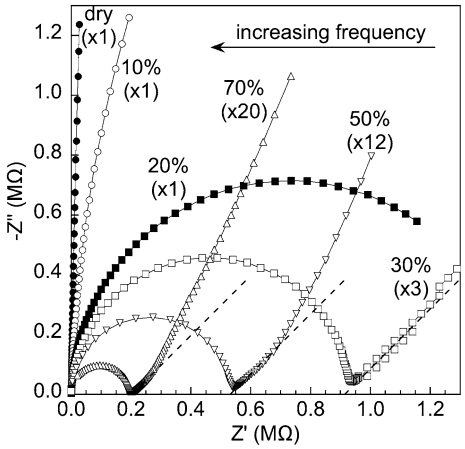

Fig. 3 Nyquist plots obtained at different RH values: dry air (●), 10% (○), 20% (■), 30% (□), 50% (▽), and 70% (△). In order to be included in the same graph, both Z' and Z'' have been multiplied by appropriate factors (in parentheses). Relevant RH values are also indicated. *Dashed lines* are straight lines having slope 1

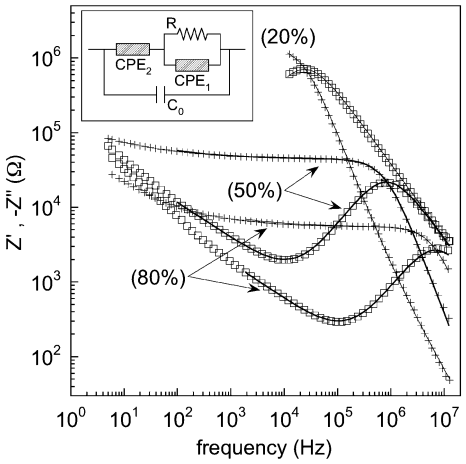

Fig. 4 Representative Z' and Z'' spectra obtained at the RH values reported in parentheses. Symbols indicate the measured real (+) and imaginary (□) parts of the impedance. *Lines* are the best fit simulations achieved by the parameters reported in Table 1. The *inset* shows the equivalent circuit used to model the sensor

only a minor arc is observed at low RH values (RH $\leq$ 20%). At intermediate frequencies, for sufficiently high relative humidity (RH $\geq$ 30%), a straight segment appears in the Nyquist diagrams at an angle of about 45° to the real axis, that is almost independent of RH. Finally, when RH $\geq$ 30% the complex impedance spectra show at low frequencies a smooth increase of Z'' vs. Z' slope. Similar behaviors have been reported for humidity sensors based on titania thick films [15], $BaTiHO_3$/polymer composite materials [16] and π-conjugated polymers [17]. Skewed semicircles are usually modeled through the parallel combination of an ideal resistor, R, and a "non-Debye" capacitor [18]. In such circuits the resistance represents a conductive path, while the dispersive capacitor is generally related to nonlocal processes and is represented by a constant phase element (CPE). The CPE is a nonintuitive circuit element whose impedance is $Z_{\mathrm{CPE}} = [\mathrm{j}\omega C_{\mathrm{n}}(\omega)]^{-1}$, where j is the imaginary unit, $\omega = 2\pi f$ the angular frequency, and $C_{\mathrm{n}}(\omega)$ the non-Debye capacitance defined as [19]

$$C_{\mathrm{n}} \equiv A(\mathrm{j}\omega)^{n-1} = A\omega^{n-1}\left[\sin\left(n\frac{\pi}{2}\right) - \mathrm{j}\cos\left(n\frac{\pi}{2}\right)\right]. \quad (1)$$

In this equation, A is the CPE coefficient with dimensions Fs^{n-1}, while n is the CPE exponent that ranges from 0 to 1, depending on the nature of the system and on the dispersion of its physical properties [18] ($n = 1$ for an ideal capacitor). Although physical interpretations of the CPE have been proposed even recently [20], no accepted theory of ac conduction exists which establishes universal relationships between the material properties and the parameters A and n.

A second constant phase element having $n \approx 0.5$ is used to model the 45° straight segment observed in the intermediate frequency range of the Nyquist diagrams, which is generally considered as indicative of a Warburg-type response, i.e., of a diffusion charge transport [21]. As for the increase of Z'' vs. Z' slope at the low frequencies, the origin of this nonlinear behavior is not definitely ascertained. Steeper Warburg-type regions have been observed at low frequencies and have been ascribed to film roughness [22] and inhomogeneity [23]. On the other hand, it has been established that a CPE-like response can be well approximated only over a limited frequency range [21]. In the present contest, we are not further discussing the impedance data from the ultimate low frequency range of the spectra.

By analyzing the Nyquist plots, we got the indication that an equivalent circuit suitable for modeling the impedance measurements should comprise the parallel combination of an ideal resistor and a constant phase element, CPE_1, in series with a second CPE, CPE_2 [24]. We considered several of such equivalent circuits and found they could partially model the experimental data in either restricted frequency ranges or limited RH conditions. Following the criterion of simplicity, we choose the equivalent circuit shown in the inset of Fig. 4 because it allows the fitting of both Z' and Z'' vs. f at all the RH values. Data from the low frequency range where the slope of the Z'' vs. Z' plot was observed to increase were not used in the fittings.

Least square fittings were carried out considering the logarithms of Z' and Z'' in order to ensure equal weighting of data over the whole range of impedance values. For each RH the fitting quality was evaluated through both the coefficient of determination of the real component (R2r) and that of the imaginary one (R2i). In particular we accepted as suitable those parameter sets that result in the largest values of the sum R2r + R2i. When different sets were found to give comparable R2r + R2i values, the one giving the lowest |R2r − R2i| was selected as the best fitting one, so that

Table 1 Values of the equivalent circuit parameters for different RHs

RH	R (Ω)	n_1	A_1	n_2	A_2	C_0 (pF)
0	$>1 \times 10^{10}$	0.800	3.46×10^{-12}			4.0
10	1.50×10^{7}	0.657	3.20×10^{-11}			4.0
20	1.47×10^{6}	0.812	6.10×10^{-12}			4.0
30	3.10×10^{5}	0.854	3.36×10^{-12}	0.443	1.10×10^{-6}	4.0
40	1.17×10^{5}	0.738	1.90×10^{-11}	0.464	1.78×10^{-6}	4.0
50	4.47×10^{4}	0.704	3.04×10^{-11}	0.468	2.85×10^{-6}	4.0
60	1.88×10^{4}	0.605	1.82×10^{-10}	0.499	3.00×10^{-6}	4.0
70	9.96×10^{3}	0.567	3.81×10^{-10}	0.501	3.89×10^{-6}	4.0
80	5.51×10^{3}	0.530	8.61×10^{-10}	0.485	5.40×10^{-6}	4.0

a good fitting of both real and imaginary components was preferred to one excellent and the other only reasonable. Following this approach, no problem concerning parameter identification was met for all the measurements here considered. The parameter values obtained are shown in Table 1. It should be specified that the 4.0 pF value reported for C_0 was forced since using C_0 as a free parameter results in values ranging from 3.6 to 4.2 pF, but at high RHs in few cases negative C_0 values were obtained. Forcing the value of 4.0 pF was found to give the best fitting results in the whole RH range. Such value of C_0 indicates that the parallel capacitance C_0 (inset of Fig. 4) corresponds to the vacuum capacitance. Figure 4 points out the correct matching of the experimental data and the best fitting curves calculated through the parameters reported in Table 1. The proposed circuit quantitatively accounts for the large resistance observed under dry-air conditions. Indeed the R value determined through the fitting at RH = 0 ($R > 10^{10}$ Ω) fairly agrees with the 9×10^{10} Ω value we calculated from the d.c. resistivity (1.4 MΩ cm) measured at room temperature and under vacuum in $MaSnCl_3$ films [12].

The parameters of Table 1 quantitatively describe the modifications of the circuit elements as a function of the relative humidity. In particular, the slight increase of n_2 with increasing RH indicates that the constant phase element CPE_2 tends to an ideal Warburg element ($n = 0.5$) when humidity increases. Due to the increase of both n_2 and A_2 the capacitance magnitude, $|C_{n_2}|$, increases as RH^2 by a factor of ∼7 when RH is increased from 30% to 80% (Fig. 5). As for the high frequency impedance, n_1 and A_1 show definite trends only for RH ≥ 30%. In particular, A_1 increases with increasing humidity while n_1 decreases, which means that the dispersive character of CPE_1 is larger the larger RH. The combined variations of n_1 and A_1 make $|C_{n_1}|$ increase almost exponentially by a factor of about 14 when RH increases from 30 to 80% (Fig. 5). Hence, both CPE_1 and CPE_2 are much less humidity sensitive than the resistance R, which strongly depends on RH. It decreases by more than three orders of magnitude when relative humidity increases from 10% to 80%. This proves that the main

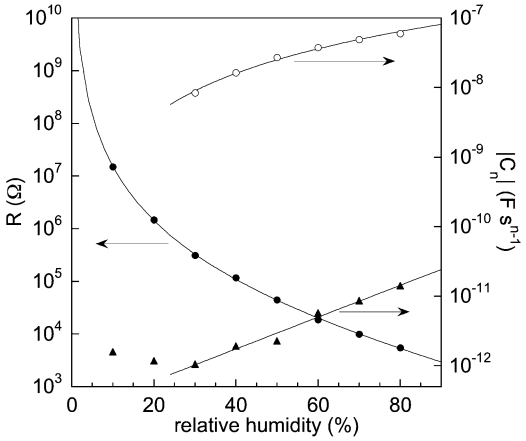

Fig. 5 Influence of relative humidity on R (●), $|C_{n_1}|$ (▲) and $|C_{n_2}|$ (○). C_{n_1} and C_{n_2} have been calculated at 1 kHz through (1) by using the parameters reported in Table 1

effect of humidity on current transport applies to the resistance R, whose logarithm does not vary linearly with RH, but decreases faster in the low RH range. Qualitatively similar behaviors of R and C were reported for humidity sensors based on titania thick films [25], where the highly humidity-sensitive resistance and less sensitive capacitance were discussed in terms of ionic charge transport in surface-adsorbed water layers. In the case of nanocrystalline TiO_2 thin films, humidity sensors were modeled [26] through an equivalent circuit very similar to the one we used. R and CPE_1 (namely the high frequency semicircle in the Nyquist plot) were attributed to a surface physisorbed water layer, while the "non-Debye" capacitance CPE_2 (i.e. the ∼45° spur) was ascribed to electrode–electrolyte polarization, although its dependence on RH was not discussed.

The role of surface adsorbed water is well recognized in ceramics [27], whose impedance sensitivity to humidity is generally related to water molecules physisorbed at the surface where they are weakly bound and can be easily removed by decreasing RH, as pointed out by the rather quick impedance changes observed in well conceived sensors. On the other hand, the well reproducible results we

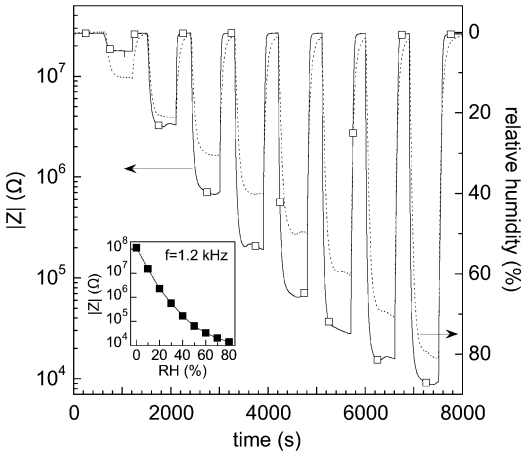

Fig. 6 Typical dynamic response measured as a function of different humidity steps at and 1.2 kHz (○). The response of a commercial sensor set nearby the sample (*dashed line*) is shown as a benchmark. *Inset* shows the impedance $|Z|$ as a function of RH

described so far refer to stationary humidity conditions and give little guidance as to the mechanisms that cause the observed impedance dependence on humidity. In order to clarify the physical origin of the above results, we studied the dynamic response of the device to RH modulations. Figure 6 shows that large and reversible variations of the a.c. current (I_{ac}) are observable for the device undergoing a sequence of humidification-dehumidification cycles in the 0–80% RH range. The current fluctuations observed during humidification likely originate from the ±1.5% humidity instabilities occurring in the test chamber under nonstationary conditions, as it is pointed out by the response of the commercial sensor (Fig. 6). In particular, if allowance is made for chamber humidity fluctuations, when RH is repeatedly varied between dry-air conditions and RH = 60% (Fig. 6) the $1/e$ response and recovery times were estimated to be ∼74 s and ∼3 s, respectively. The response time is slightly larger than that of the commercial sensor (∼52 s), while the recovery time is much shorter than both the response time and the commercial sensor recovery time. When RH is varied between 0 and 80%, a $1/e$ rise time of about 85 s and a fall time of about 10 s are estimated. These rise-time values have been observed to be rather reproducible in several devices, although times as long as 120 s were measured in few cases. On the other hand, fall time does not vary appreciably from device to device. To explain this behavior we should consider that any comparison with the recovery of the commercial sensor is made difficult by its position in the chamber. Indeed, when the sensor was set in the place of the test device its fall time was comparable to the nominal one which is 15 s. This result and the nearly constant fall times we observed on different devices suggest that measured recovery may be affected by the chamber reaction time. Thus, we can conclude that the recovery of the devices under test is so fast that reported fall times should be considered as the upper time limit for the device under test.

The relatively short response times and, mostly, the very short dehumidification times would reasonably support the hypothesis that current changes are related to surface mechanisms, likely involving water molecules loosely bound at the surface of the $MaSnCl_3$ films. A plausible mechanism could be analogous to the one first proposed for silica gel [28] and used also for perovskite [29] and porous oxides [25]. It assumes that the humidity dependent conduction is of a protonic nature [30] and originates from the physisorption of water molecules on anchor points such as surface hydroxyls and water ligands. In particular, at low humidity (adsorbed layer less than one monolayer) conduction is due to H_3O^+ ions, while when humidity increases (adsorbed layer greater than one monolayer), the dominant charge carriers are protons, H^+, that move freely in water layers showing a liquid-like behavior, according to the Grotthuss proton transmission mechanism [28].

Following this model, we can tentatively interpret our results considering that (1) charge conduction takes place in physisorbed water layers, where H_3O^+ and H^+ are the main charge carriers at low RH and medium to high RH, respectively. Since H^+ ions are more mobile than H_3O^+ and the concentrations of mobile charge carriers increase with H_2O adsorption, the resistor R decreases when RH increases due to increasing charge carrier concentration and mobility. (2) CPE_1 originates from water molecule polarization effect that is enhanced when RH increases in the medium to high humidity range [29]. This would explain the increase we observed in C_{n_1} for RH ≥ 30% (Fig. 5). (3) Since gold contacts are ion-blocking electrodes [29], charged ions are expected to accumulate at the electrodes causing space charge polarization that increases when increasing humidity, thus Inducing the increase of C_{n_2}. Thus, the results we have reported can be qualitatively interpreted in terms of protonic conduction in layers of water physisorbed on the surface of the $MaSnCl_3$ films.

As a final comment, we note that the device response is quite reproducible on the time scale of a few days. This is well demonstrated in Fig. 7 where we show the I_{ac} values measured on the same sample during two humidification-dehumidification experiments (0–60% RH range). The experiments were carried out before and after 72 hours working at RHs ranging from 30% to 80%. The two response curves can hardly be distinguished from each other, thus proving the device stability. This result is consistent with the X-ray diffraction experiments (Fig. 1) and suggests that $MaSnCl_3$ may be considered for use in humidity sensing devices. Work is under way to verify the device stability on longer time scale.

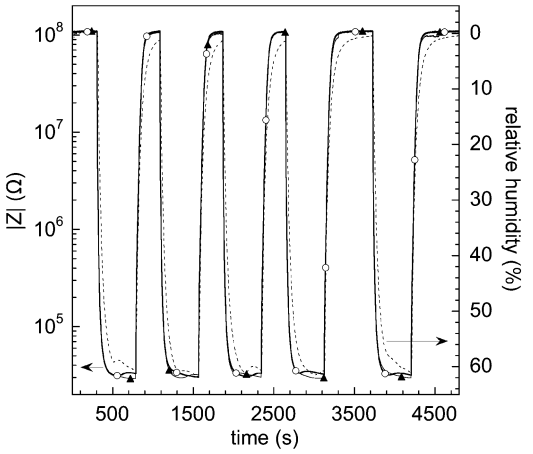

Fig. 7 Response and recovery curves measured at 120 Hz during two sequences of humidification–dehumidification cycles before (○) and after (▲) 72 hours working at RHs ranging from 30% to 80%. The response of the commercial sensor (*dashed line*) is shown as a reference

4 Conclusions

The complex impedance of $MaSnCl_3$ hybrid films has been shown to depend on humidity. Interdigitated two-electrode devices have been modeled in the whole 0–80% relative humidity range by a rather simple equivalent circuit comprising one resistance and two constant phase elements. The stationary humidity characteristics demonstrated that impedance variations as a function of RH are mainly due to the resistive component of the circuit, which decreases by more than three orders of magnitude when RH increases from dry-air to 80%. Dynamic responses of the devices during humidification–dehumidification cycles showed large and fast variations of the current, with rise times of few hundred seconds and fall times as short as few tens of seconds. This suggests that sensitivity to humidity originates from mechanisms involving water molecules physisorbed on the film surface.

The results obtained were quite reproducible when measured on different samples or on the same sample during several working days. These observations hint that $MaSnCl_3$ films could be envisaged as the active layer of hybrid humidity sensing devices.

Acknowledgements Thanks are due to J.J. Mares and P. Hubik for useful discussions. This work was partially supported by the PROMINER/MISTER Laboratory.

References

1. D.B. Mitzi, in *Functional Hybrid Materials*, ed. by P. Gomez-Romero, C. Sanchez (Wiley-VCH, Weinheim, 2004), p. 347
2. D.B. Mitzi, J. Chem. Soc., Dalton Trans. **2001**, 1 (2001)
3. K. Yamada, T. Matsui, T. Tsuritani, T. Okuda, S. Ichiba, Z. Naturforsch. A **45**, 307 (1990)
4. D.B. Mitzi, C.A. Field, Z. Schlesinger, R.B. Laibowit, J. Solid State Chem. **114**, 159 (1995)
5. T. Matsushima, K. Fujita, T. Tsutsui, Jpn. J. Appl. Phys. **45**, 523 (2006)
6. N. Onoda Yamamuro, T. Matsuo, H. Suga, J. Chem. Thermodyn. **23**, 987 (1991)
7. K. Yamada, Y. Kuranaga, K. Ueda, S. Goto, T. Okuda, Y. Furukawa, Bull. Chem. Soc. Jpn. **71**, 127 (1998)
8. I. Borriello, G. Cantele, D. Ninno, Phys. Rev. B **77**, 235214 (2008)
9. D.B. Mitzi, Prog. Inorg. Chem. **48**, 1 (1999)
10. K. Yamada, H. Kawaguchi, T. Matsui, Bull. Chem. Soc. Jpn. **63**, 2521 (1990)
11. F. Chiarella, P. Ferro, F. Licci, M. Barra, M. Biasucci, A. Cassinese, R. Vaglio, Appl. Phys. A **86**, 89 (2007)
12. F. Chiarella, A. Zappettini, F. Licci, I. Borriello, G. Cantele, D. Ninno, A. Cassinese, R. Vaglio, Phys. Rev. B **77**, 45129 (2008)
13. D.B. Mitzi, Chem. Mater. **13**, 3283 (2001)
14. C. Aruta, F. Licci, A. Zappettini, F. Bolzoni, F. Rastelli, P. Ferro, T. Besagni, Appl. Phys. A **81**, 963 (2005)
15. P.M. Faia, C.S. Furtado, A.J. Ferreira, Sens. Actuators B **107**, 353 (2005)
16. J. Wang, Q. Lin, R. Zhou, B. Xu, Sens. Actuators B **81**, 248 (2002)
17. E. Quartarone, P. Mustarelli, A. Magistris, M.V. Russo, I. Fratoddi, A. Furlani, Solid State Ion. **136–137**, 667 (2000)
18. A.K. Jonscher, Phys. Status Solidi A **32**, 665 (1975)
19. J.R. Macdonald, Solid State Ion. **13**, 147 (1984)
20. M.R. Shoar Abouzari, F. Berkemeier, G. Schmitz, D. Wilmer, Solid State Ion. **180**, 922 (2009)
21. J.R. Macdonald, D.R. Franceschetti, in *Impedance Spectroscopy*, ed. by J.R. Macdonald (Wiley, New York, 1987), p. 84
22. G. Lang, G. Inzelt, Electrochim. Acta **36**, 847 (1991)
23. I. Rubinstein, J. Rishpon, S. Gottesfeld, J. Electrochem. Soc. **133**, 729 (1986)
24. J.F. McCann, S.P.S. Badwal, J. Electrochem. Soc. **129**, 551 (1982)
25. P.M. Faia, C.S. Furtado, A.J. Ferreira, Sens. Actuators B **101**, 183 (2004)
26. K.P. Biju, M.K. Jain, Thin Solid Films **516**, 2175 (2008)
27. N. Yamazoe, Y. Shimizu, Sens. Actuat. 10, 379 (1986)
28. J.H. Anderson, G.A. Parks, J. Phys. Chem. **72**, 3362 (1968)
29. Y.C. Yeh, T.Y. Tseng, J. Mater. Sci. **24**, 2739 (1989)
30. T. Norby, Solid State Ion. **125**, 1 (1999)